Dynamic damage response of sing-crystal NiTi alloys induced by shear localization

Yuchen Zhang[1], Weilong Yang[1], Xin Yang[2], Jin Wang[3], Chao Lv[4], Hao Zhang[4],
Xiaoyang Pei[4*], and Fang Wang[1*]

[1] School of Materials and Energy, Southwest University, Chongqing 400715, China;

[2] Shock and Vibration of Engineering Materials and Structures Key Laboratory of Sichuan Province, School of Environment and Resource,
Southwest University of Science and Technology, Mianyang 621010, China;

[3] State Key Laboratory of Nuclear Physics and Technology, Center for Applied Physics and Technology, Peking University,
Beijing 100871, China;

[4] Institute of Fluid Physics, China Academy of Engineering Physics, Mianyang 621999, China

This work investigates the dynamic response of a monocrystalline nickel-titanium (NiTi) alloy at the atomic scale. The results deduced from non-equilibrium molecular dynamics modeling demonstrate that no shear deformation band (SDB) appears in the sample at an impact velocity of less than 0.75 km/s. As this velocity increases, shear deformations become pronouncedly localized, and the average spacing between SDBs decreases until it stabilizes. Combining shear stress and particle velocity profiles, the survival of SDBs is found to be closely associated with plastic deformation. The dislocations clustering around SDBs predominantly exhibit ⟨100⟩ partial dislocations, whereas $1/2\langle111\rangle$ full dislocations are dominant in those regions without SDBs. Void nucleation always occurs on SDBs. Subsequently, void growth promotes a change in the SDB distribution characteristic. For the case without SDB, voids are randomly nucleated, and the void growth exhibits a non-uniform manner. Thus, there is an interaction between shear localization and void evolution in the NiTi alloy subjected to intensive loading. This study is expected to provide in-depth insights into the microscopic mechanism of NiTi dynamic damage.

NiTi alloy, Shear deformation band, Void nucleation and growth, Plasticity, High strain rate

1. Introduction

In the past few decades, intensive concerns have been focused on the development of superior materials for utilization in many industrial applications. High-performance metals and alloys exhibit excellent dynamic performance together with superior ductility and strength under intensive impact loading. They are among the most promising candidates for structural components in fields such as civil defense, automobile, and aerospace [1-3]. Under such extreme conditions, materials are usually deformed to large

plastic strains generated by loading, and they are in a non-equilibrium state during the response time [4]. Consequently, it promotes the formation of zones of localized shear deformation, which can act as loci for the initiation of voids and cracks. With continuous damage accumulations, these defects quickly expand along the boundary of the plastic zone or its interior, leading to a sudden failure of materials [5]. It is, therefore, imperative to deepen our comprehensive understanding of the shear instability and its mechanism during dynamic damage.

Much effort has been devoted to the study of dynamic behavior with shear localization using experimental characterization. Wei et al. [6] conducted experiments and reported that plastic deformation-induced high strength and

Y. Zhang, *et al. Acta Mech. Sin.*, Vol. 41, 124177 (2025)

124177-2

reduced strain hardening were favorable to the onset of adiabatic shear localization. Zhao [7] performed a Hopkinson bar experiment to investigate the shear banding mechanism of metals, revealing the strong dependence of the formation of shear bands on temperature and strain rate. Liao and Duffy [8] conducted dynamic torsional experiments to explore the initiation and propagation of shear bands in deformed thin-walled tubular specimens of titanium (Ti)-based alloys. Importantly, local strain, temperature profile, and material performance during shear band formation were also determined. Additionally, Ma et al. [9] discovered the shear banding deformation and failure mechanism of pure Ti through direct quantitative measurement, offering valuable insights into the microstructure evolutions required for shear banding.

Because of the challenges posed by experimental techniques in detecting variables within the short-history and small-scale shear bands, extensive numerical simulations have been conducted to study shear banding failure and its mechanism. Wang et al. [10] used the phase-field evolution equation to simulate the formation of self-organized shear bands in a thin-walled cylinder, demonstrating that the quantity and spacing of shear bands were significantly affected by loading rate and material properties. In recent work, Zeng et al. [11] conducted an extensive investigation on dynamic shear failure. The results indicated that shear localization nucleation was primarily dominated by microstructure-dependent softening, such as dynamic recrystallization. Although there has been explosive attention focused on the shear instability of metallic materials in a couple of decades, the nature of the onset and evolution of shear localization during dynamic deformation is further being explored from the perspective of microscale.

Molecular dynamics (MD) modeling has been recognized as an effective tool for clarifying material impact response [12], which can provide microscopic insight into unique phenomena that are difficult to observe in practice. Avila et al. [13] performed MD simulations to reveal the interaction of multiple shear bands, allowing for the linkage of the structural performance of a single shear band to the presence of other subsequently generated shear bands. Xu and Chen [14] presented an atomistic-to-continuum multiscale coupling approach, and they used atomic potential-based energy fluxes to determine the onset of shear instability. The results demonstrated that dislocation interactions promoted the initiation of the shear instability process, highlighting the importance of microstructural evolution to dynamic shear banding. There are complicated microstructure evolutions in metals during intensive shock, which renders it challenging to examine the influence of shear deformation on dynamic performance. Holian and Lomdahl [15] provided an in-depth understanding of shock-induced plasticity in face-centered cubic crystals, underscoring the richness of nanostructures behind

the slippage. By constitutive modeling, Gurrutxaga-Lerma [16] provided a physical description of the dislocation dynamics, highlighting the importance of the interplay between dislocation generation and motion in promoting the development of shear banding in crystalline metals. Typically, ductile damage evolution is characterized by void nucleation, growth, and coalescence [17,18]. Wu et al. [19] found that the shear strain near voids tended to activate dislocation motions and shear banding formation. Furthermore, Kubair et al. [20] studied the formation of multiple shear bands in ductile materials, indicative of a shear-void-growth softening effect during dynamic damage. To date, the mechanism behind the interaction between voids and shear localization remains inconclusive and deserves to be further explored.

Nickel-titanium (NiTi) alloys have been commonly used in fields such as biomedical, aerospace, automotive, and intelligent machines because of their exceptional superelasticity, good biocompatibility, shock resistance, chemical corrosion resistance, and shape memory effect [21]. NiTi and its components often have to encounter the risk of hyper-velocity impact [22]. Thus, there is an urgent need to understand the basic mechanics of dynamic damage. It is known that NiTi alloys possess unique mechanical properties under strong impact loading, completely different from those of other ductile metals. For example, Zhang et al. [23] reported that there was almost no phase transition observed in NiTi alloys under a high strain rate, compared to other body-centered cubic-based metals that undergo a remarkable crystal structure transition [24]. Moreover, some studies reported that voids were likely to be nucleated at the regions with high dislocation density for tantalum [25] and copper [26]. In contrast, Wu et al. [27] revealed an exceptional plasticity mechanism of NiTi alloys during damage accumulation. Very few studies have focused on the NiTi dynamic performance by considering shear localization at the atomic scale.

In this work, the dynamic damage evolution of a NiTi alloy at a high strain rate was reproduced using non-equilibrium molecular dynamics (NEMD) simulations. The evolution of shear deformation was investigated by considering the shear deformation band (SDB) distribution. Dislocation activities around SDB were also examined. Importantly, the statistics of dislocation and void profiles were analyzed to explore the shear deformation broadening and its mechanism during microstructure evolution. The present study is expected to gain new insights into dynamic performance caused by shear localization.

2. Simulated details

Many studies have shown that the embedded-atom method (EAM) potential is well suited to represent the interactions

between individual atoms in multicomponent systems, such as NiTi alloys [28,29]. As presented in Table 1 [28,30-33], we also calculated several physical properties to compare computational results and experimental data, demonstrating that this potential could be used to reproduce the NiTi shock response in the present study.

It is well known that an impact procedure always satisfies the conservations of mass, momentum, and energy of the system, which complies with NEMD simulations [34]. Accordingly, this work conducted large-scale NEMD simulations to investigate complex mechanisms behind shock wave propagation, plastic deformation, and dynamic damage. The whole simulated procedure was accomplished using the open-source large-scale atomic/molecular massively parallel simulator software [35].

Figure 1 displays the NiTi configuration for subsequent simulations. In an initial crystal, the B2 austenite phase has a crystal lattice constant of 3.008 Å. For analytical simplicity, the system is composed of 248 × 70 × 49 B2 unit cells. Therefore, the entire MD model has dimensions of 1,070 Å × 211 Å × 208 Å along the X-, Y-, and Z-axes, respectively, consisting of 3,409,420 atoms. The simulated system was divided into a piston 15 Å in length and a target with a size of 1,055 Å along the X-axis direction. As presented in Fig. 2, $Ni_{52}Ti_{48}$ was achieved by randomly replacing some Ti atoms with Ni atoms in the nanocrystalline $Ni_{50}Ti_{50}$. It is worth noting that Refs. [23,36] have also proved that the EAM potential could be availably applicable to the dynamic response simulation for $Ni_{52}Ti_{48}$.

Then, in the simulation, the [110], [001], and [1$\bar{1}$0] orientations were placed along the X-, Y-, and Z-axes, respectively, of the Cartesian reference frame. For the removal of the edge effect, the system remained free along the shock direction (X-axis), and the Y- and Z-axes directions were subjected to periodic boundary conditions.

When the model was constructed, the system energy was minimized using the well-known conjugate gradient method [37]. Afterward, the relaxation of the model with a three-dimensional periodic boundary was performed under an initial temperature of 300 K and zero pressure with an isobaric-isothermal ensemble (NPT) for 30 ps until an equilibrium state was reached to eliminate the effect of residual stress. By considering no heat exchange between the preset impact process and surroundings, a microcanonical ensemble (NVE) was used to simulate the NiTi shock behavior [38]. In this study, shock waves in simulated samples were
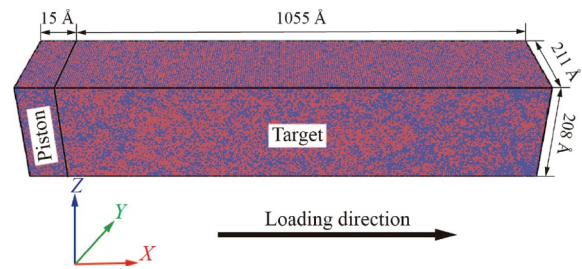

Figure 1 Schematic of the simulated specimen under piston loading.
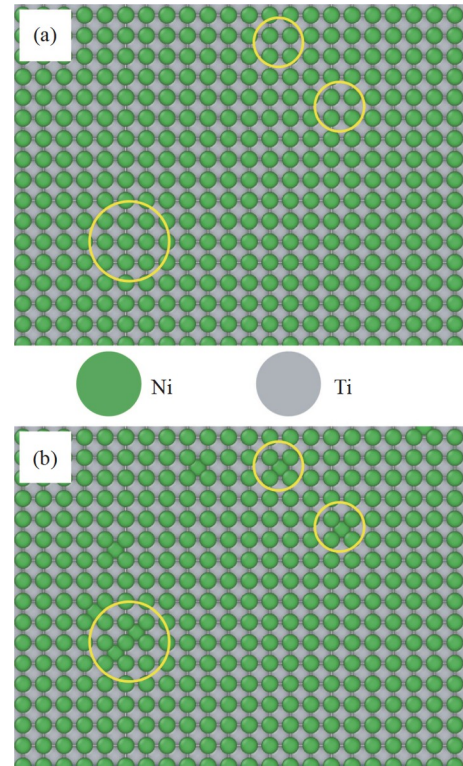

Figure 2 Local views of the simulated alloy (a) before and (b) after the Ni atom substitution, where green and gray atoms denote Ni and Ti atoms, respectively.

generated using the piston method [39], in which atoms inside a thick plate at the left end of the system were regarded as the piston, as displayed in Fig. 1. During shock loading, the target with a static state was impacted by moving the rigid piston at a certain impact velocity (U_P) ranging from 0.5 to 1.6 km/s. It should be mentioned that the loading process lasted 15 ps, followed by an unloading duration of 50 ps. All the simulations were implemented with a time step of 0.001 ps for relaxation, shock com-

Table 1 Comparison of predicted and experimental physical properties of the NiTi alloy with B2 phase

Physical property	Elastic constant (GPa)			Lattice constant (Å)	Bulk modulus (GPa)	Cohesive energy (eV)
	C_{11}	C_{12}	C_{44}			
Present potential	227	146	46	3.008	134	−5.02
Other work	183 [30]	146 [30]	46 [30]	2.999 [31]	159 [32]	−5.05 [31]
Experiments	162 [33]	129 [33]	35 [33]	3.008 [28]	140 [33]	−5.02 [28]

pression, and release. Additionally, transient responses, such as velocity, shear strain, and pressure, were taken as a function of coordinate and time for the binning analysis. The target was divided into a substantial amount of bins along the shock direction and each bin had three unit cells (9.024 Å) in width [40].

During simulations, local structural environments were visualized using the open visual viewer OVITO to identify microstructure evolutions. For a given material system, the shear strain was identified using the atomic strain method, in which the atomic-level deformation gradient and the strain tensor at each particle could be derived from the relative motion of neighboring particles [41]. Because the advantage of the dislocation extraction algorithm is that it can recognize partial dislocations and interfacial dislocations in defective atomic structures, such a method was adopted to diagnose dislocation structures and their evolutions [42], allowing us to explore the plastic deformation mechanism. Moreover, void statistics were accomplished with the help of the construct surface mesh method based on the Alpha-shape algorithm, which can efficiently count the surface area, solid volume, and porosity of atomic structures [43].

3. Result and discussion

3.1 Formation and propagation of SDB

In this part, the simulated system was shocked under uni-axial impact to explore SDB evolution. Figure 3 presents the shear strain distribution within the sample in addition to
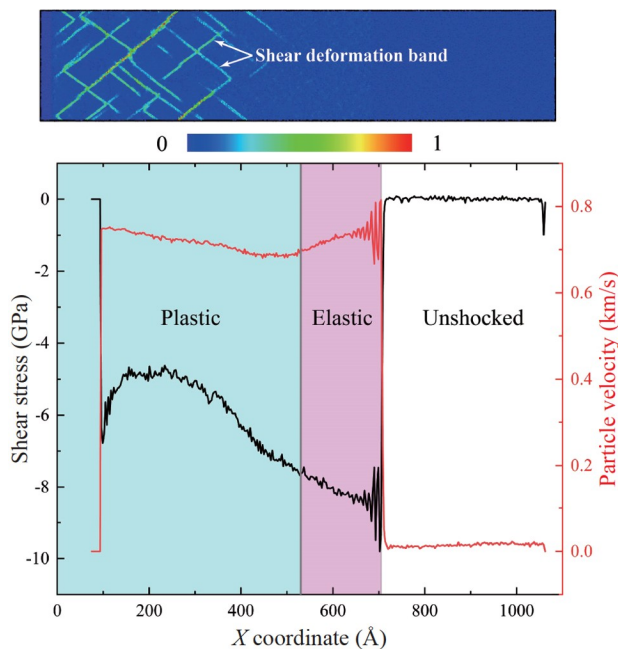

Figure 3 SDB distribution colored according to shear strain, together with shear stress and particle velocity profiles when the impact velocity is 0.75 km/s.

shear stress and particle velocity profiles at 10 ps for an impact velocity of 0.75 km/s. The material was divided into plastic, elastic, and unimpacted regions along the shock wave propagation. From this, it was discovered that the elastic wave speed is higher than the plastic wave speed at the propagation distance. The inhomogeneous oscillation in the front of the shock wave in the elastic region is caused by an elastic precursor. Moreover, we discovered that there are many strip-shaped bands covered by high shear strain in the plastic region. The presence of a plastic zone is expected as the result of the continuous loading of the shock pulse [44]. Accordingly, the SDBs were produced during the propagation of the plastic excitation wave, corresponding to the plastic region. This will be discussed in the subsequent analysis.

Figure 4 displays the SDB distribution colored according to shear strain at several velocities. For an impact velocity of 0.5 km/s, no significant shear strain concentrations occur in the material. Interestingly, when the impact velocity reaches 0.75 km/s, some strip-like high shear strain zones with certain angles are regularly distributed, demonstrating that the shear formation bands are produced. It needs to be mentioned that such events are not stacking faults [45,46], which can be identified by the common neighbor analysis. As an impact velocity continuously increases, more SDBs with a striped manner can be observed, indicative of the SDB multiplication. In this work, 0.75 km/s was considered the characteristic impact velocity for promoting the occurrence of SDB in the NiTi alloy under intensive shock.

Figure 5 presents the evolution of SDBs during impact loading. It can be observed that the SDBs are generated at the left end (1 ps). With the impact proceeding, the incident wave propagates toward the right side along the shock direction, and in turn, the SDBs gradually expand toward the central area, leading to a wider distribution region. When the
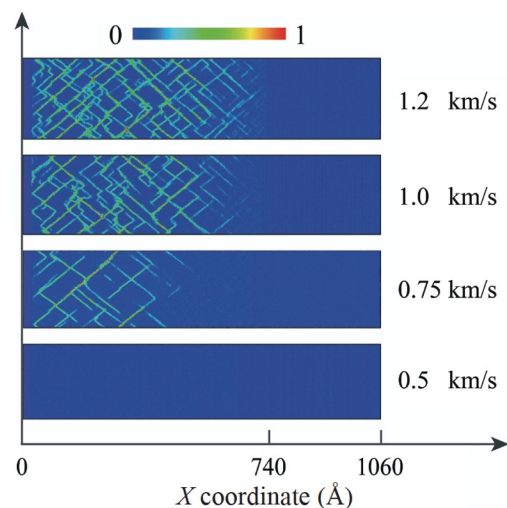

Figure 4 SDB distribution colored according to shear strain in the NiTi alloy at 10 ps when the impact velocity is 0.5, 0.75, 1.0, and 1.2 km/s.
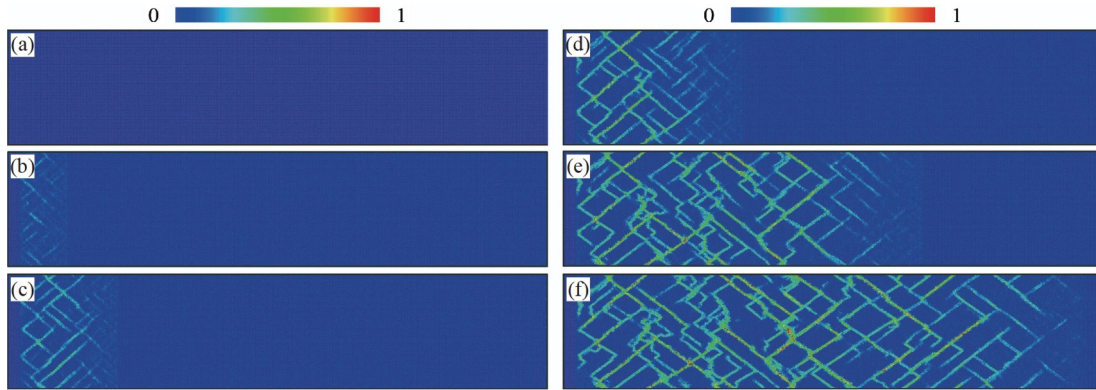
Figure 5 Profiles of SDB at (a) 0, (b) 1, (c) 3, (d) 5, (e) 10, and (f) 15 ps, when an impact velocity is 1.0 km/s.

impact loading is terminated (15 ps), there is a maximum SDB distribution domain present in the material.

Figure 6 illustrates the SDB distribution in the system at 1.0 km/s (marked by a white dashed line). We observed that the SDBs are parallelly distributed in a strip-like manner. To explore the SDB evolution and its law, the SDB spacing is defined as a perpendicular distance between the two closest SDBs. Additionally, the SDBs are likely to be arranged along a specific angle, and then the angle between SDB orientation and shock direction (X-axis) is used to represent the distribution angle. In this study, the spacing and distribution angle of SDBs were taken to characterize SDB distribution during dynamic damage [47], from the perspective of shock response. It needs to be mentioned that the spacing and angle were determined using the OVITO software.

Figure 7 displays the dependences of SDB spacing and distribution angle on impact velocity. The SDB distribution characteristics were counted within a 700-Å-width region ranging from 300 to 1,000 Å along the X-axis direction. There is a statistical distribution for SDB spacings. The relationship between average SDB spacing and impact velocity is presented in Fig. 7(a). The SDB spacing significantly decreases from 132.8 to 50.3 Å, along with impact
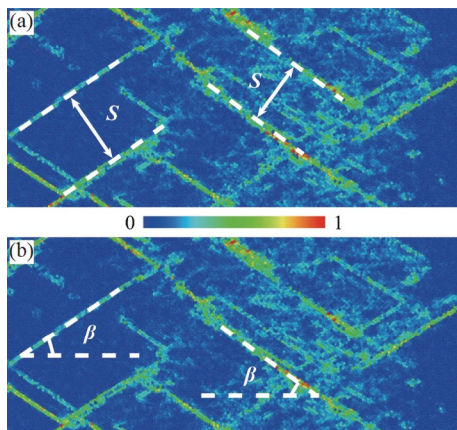
velocity increasing from 0.75 to 1.0 km/s.

Surprisingly, as the impact velocity continuously increases to 1.2 km/s, the decreasing trend for SDB spacing slows down, and the spacing becomes 30.8 Å. Moreover, when the impact velocity exceeds 1.2 km/s, the spacing of SDB remains almost unchanged. A similar behavior was observed in other materials [48].
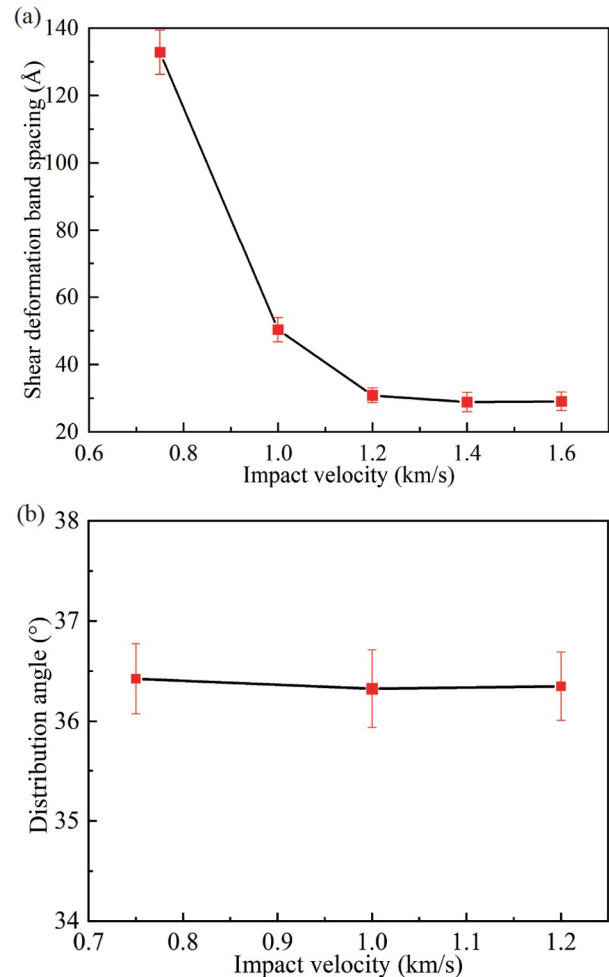

Figure 7 Dependence of (a) spacing and (b) distribution angle of SDB on impact velocity.

Figure 6 Schematic of (a) spacing and (b) distribution angle of SDB.

Figure 7(b) demonstrates the statistics of distribution angles of the SDBs. Using the visualization software, we discovered that there is no significant change in the SDB distribution angle when the impact velocity continuously increases. After the measurement, such an angle was averaged as 36.4°, which is approximately close to the [111] orientation (35.3°).

As mentioned earlier, as the shock wave propagates along the impact direction, SDBs are generated and continuously proliferate. Plastic deformation is rooted from dislocation activity [15]. To explore the dislocation evolution during shear localizations, atoms with high shear strain (beyond 0.8) on the SDBs were preserved, as displayed in Fig. 8. The SDBs started to be generated from the left side. Along with the evolution of the SDBs, dislocations were produced and clustered around the SDBs. Furthermore, we observed that the dislocations distributed in the system belong to typical $1/2\langle 111\rangle$, $\langle 100\rangle$, and $\langle 110\rangle$ types.

By counting the length of each identified dislocation type, $1/2\langle 111\rangle$ full dislocation was found to be dominant during shocking, owing to the highest percentage in comparison with other types, as presented in Fig. 9. Although $1/2\langle 111\rangle$ dislocations are prominent in NiTi alloys under intensive loading [27], massive $\langle 100\rangle$ dislocations were still observed around the SDBs. However, there are almost $1/2\langle 111\rangle$ full dislocations distributed in the regions without SDB, suggesting that the dislocation types are sensitive to SDB.

As displayed in Fig. 10, it was also found that after 15 ps, the length of $1/2\langle 111\rangle$ and total dislocations decreased, while $\langle 100\rangle$ dislocation length first increased and subsequently decreased. This was attributed to the decomposition of full dislocations into partial dislocations, leading to a sharper decrease for $1/2\langle 111\rangle$ dislocation. This phenomenon primarily occurs close to the SDB region, demonstrating that
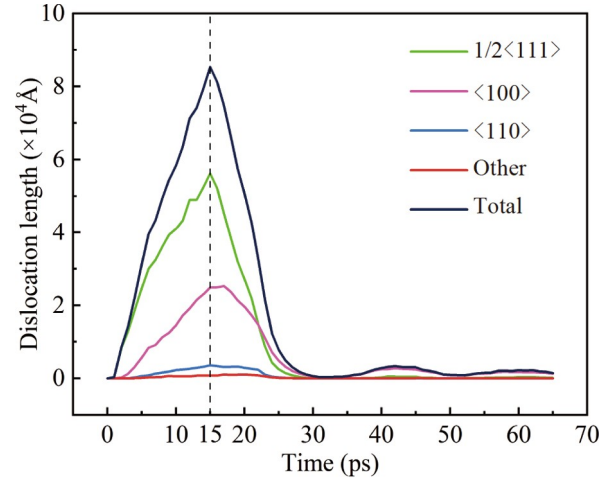
Figure 9 Dislocation length evolutions in the sample during shocking.

shear localization plays a positive role in the transformation of dislocation types.

Furthermore, the dislocation length was found to continuously increase until the SDB expands to the maximum distribution region. However, compared with 15 ps, there is no significant change in the SDB distribution pattern, whereas the dislocation length sharply decreases. This is because when the distance between dislocation lines becomes small enough, two dislocation lines with equal and opposite Burgers vectors could cancel each other and be annihilated [49].

3.2 SDB broadening during spallation

Figure 11(a) displays the pressure profile during the shock wave propagation. We observed that the waveform changed from a trapezoidal wave to a triangular one at 21 ps, suggesting that the reflected wave meets the shock wave after the former reaches the free surface.
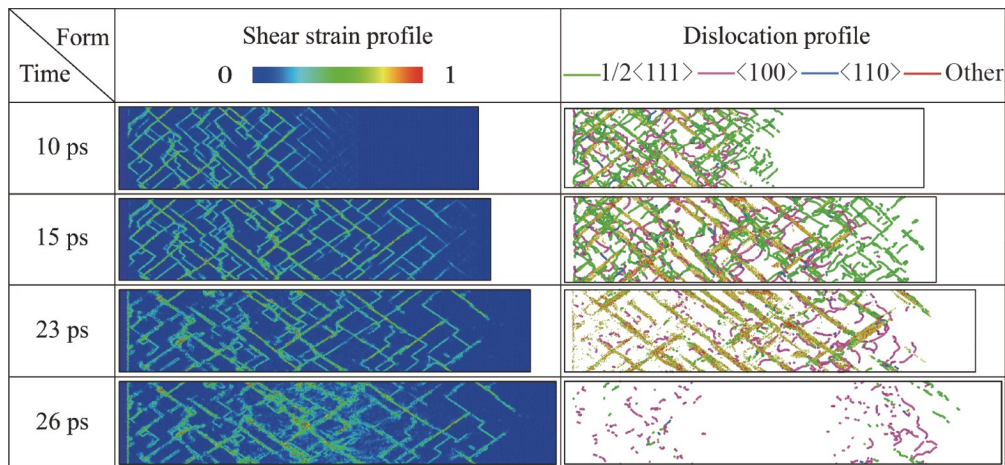
Figure 8 Schematic of the SDBs colored according to shear stress for an impact velocity of 1.0 km/s, accompanied by dislocation distributions on the SDB. Green, purple, blue, and red lines represent the dislocation types of $1/2\langle 111\rangle$, $\langle 100\rangle$, $\langle 110\rangle$, and other mismatched segments, respectively.
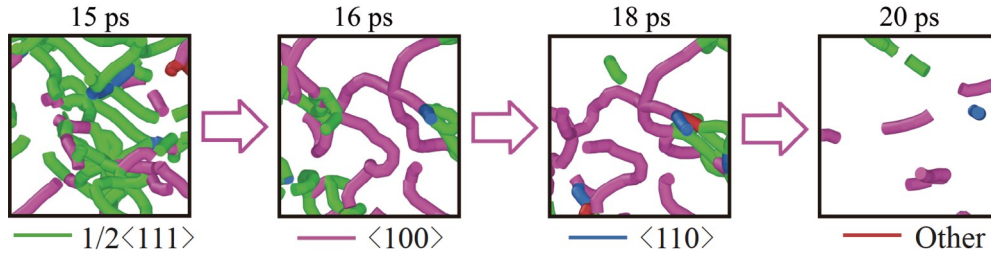
Figure 10 Local enlarged views of dislocation evolutions from 15 to 20 ps when the impact velocity is 1.0 km/s.
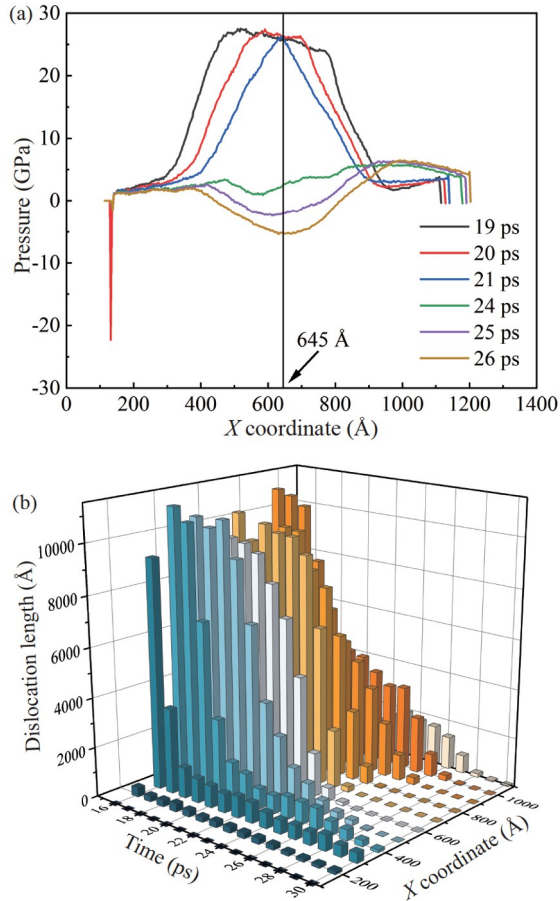

Figure 11 Evolutions of (a) pressure and (b) dislocation length over time in monocrystalline NiTi at the impact velocity of 1.0 km/s.

The interaction between these two waves is more likely to cause the dislocation line to move in the opposite direction, contributing to dislocation annihilation. Interestingly, the dislocation annihilation primarily occurs at the encountering position of the two waves (approximately 645 Å). Afterward, the intensification of such behavior leads to the minimum dislocation length at 26 ps, as presented in Fig. 11(b). When the tensile stress produced in the system continuously accumulates until reaching the spall strength, void nucleation occurs. Surprisingly, it was discovered that the region for void nucleation approximately corresponds to the region for dislocation annihilation. We believe that dislocation annihilation deteriorates the ability to resist mate-

rial damage [50], which is conducive to the occurrence of void nucleation.

Figure 12 displays the void nucleation and growth in the system when the impact velocity is 1.0 km/s. It was observed that some voids are dispersedly nucleated with a punctate shape in the dislocation annihilation regions. Moreover, all the void-nucleation sites are almost distributed in the SDB, the arrangement of which exhibits a regular behavior. Interestingly, the void nucleation and growth were found to occur along the distribution direction of SDBs (marked by a red arrow). It is worth emphasizing that the void nucleations are primarily concentrated near the center of the simulated system, because such positions could be determined by adjusting the sample size.

Figure 13 presents a comparison of the void evolution for two typical impact velocities. For 0.5 km/s, we found that there are no SDBs generated in the sample, and that void nucleations occur randomly. Thus, there was no specific path or regularity for the void nucleation and growth. Moreover, some individual voids were found to grow faster than surrounding voids (marked by a blue circle), thereby exhibiting a heterogeneous manner of growth. After the number of voids reaches the maximum value, the increase in the volume of individual voids promotes the expansion of the void distribution region [51], and void aggregation occurs between two or more voids.

Consequently, the overall volume of voids maintains an upward trend, whereas the number of voids decreases significantly, as presented in Fig. 14. It is inferred that the presence of SDBs is favorable to the formation of voids. Importantly, void evolution is likely to occur along the distribution direction of SDBs.

Figure 15 presents the evolvement of SDB behavior together with void evolution (from 28 to 34 ps). The void volume in the SDBs continuously increases, producing a wider region for void distribution.

Figure 16 demonstrates the broadening behavior of the SDB in the material from the perspective of atom motion. At 27 ps, the voids started to become nucleated, and broadening of the SDB did not occur. By tracking the movement trajectories of the selected atoms, it was clearly observed that the atoms on one SDB moved toward the closest SDB, along the distribution angle of an SDB intersected by the afore-
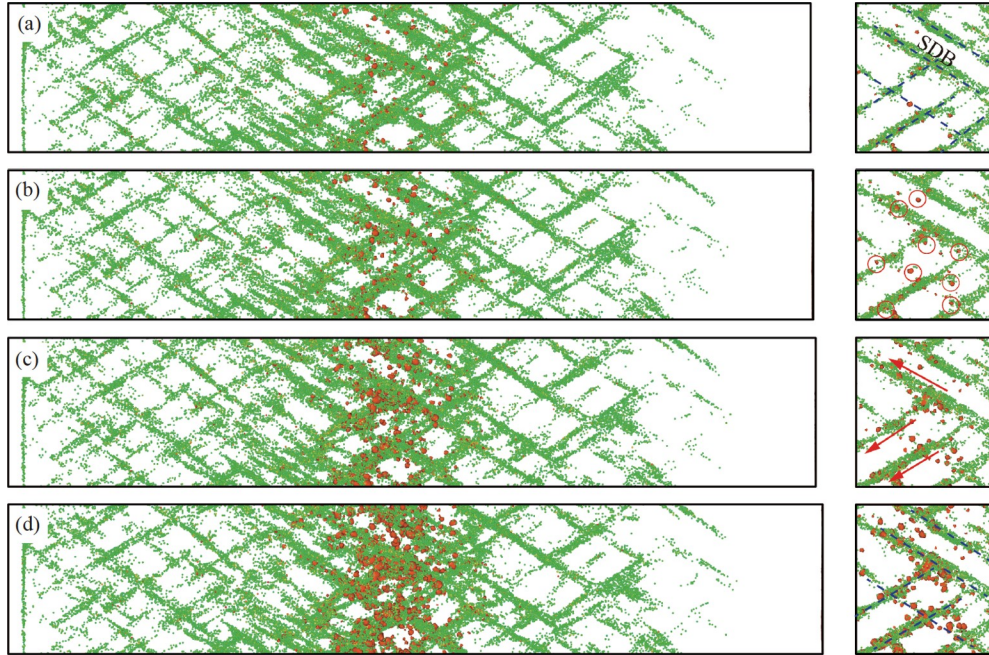
Figure 12 Schematic of void nucleation at (a) 27, (b) 27.2, (c) 27.5, and (d) 27.8 ps when the impact velocity is 1.0 km/s. The blue dashed line indicates the presence of a SDB, the red circle indicates the point distribution, and the red arrow indicates the direction of the nucleation.
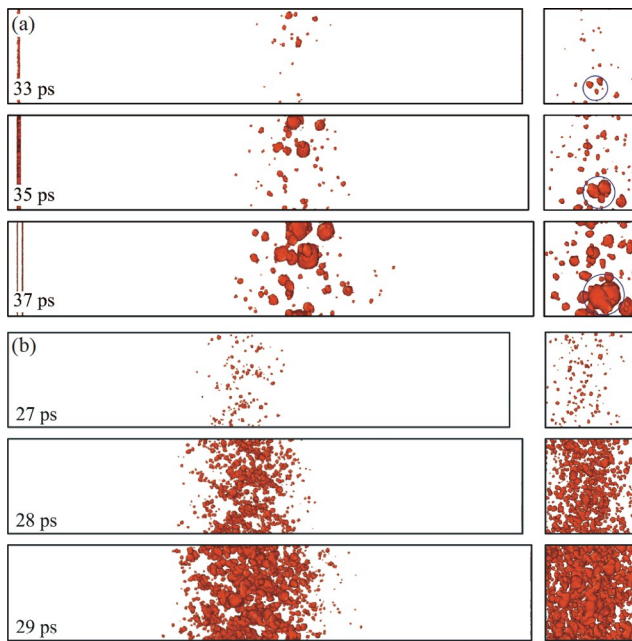

Figure 13 Schematic of void evolution pattern at (a) 0.5 and (b) 1.0 km/s.

Figure 14 Void volume and number evolutions over time in monocrystalline NiTi at the impact velocity of 1.0 km/s.

mentioned two SDBs. Consequently, the distance between the two adjacent SDBs decreased, leading to the SDB broadening. This phenomenon is expected as the result of aggregation behavior realized by atom movement.

Figure 17 displays the width profile for a specified SDB during the broadening, where the SDB width is defined as W. As accumulative voids, there are wider SDBs present in the sample, leading to a broadening behavior. Together with Figs. 14 and 15, it is believed that the void coalescence
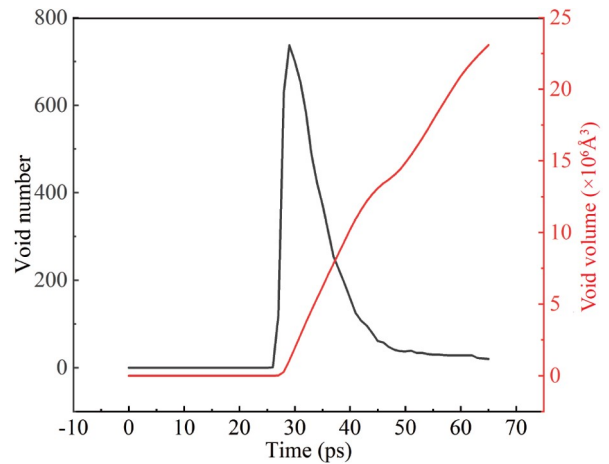
causes an increase in void volume so that the void-distributed zone is beyond the SDB.

In consequence, such an expansion pushes the atoms on the void surface outward, thereby producing a wider width of the SDB. Hence, the spacing between two adjacent SDBs becomes narrowed and eventually disappears. At this time, the SDB coalescence occurs. Along the void evolution, this effect becomes intensified, leading to the coalescence between multiple SDBs. In contrast to the previous regular strip-like distribution, the SDBs exhibit a lump-shaped distribution pattern (marked by a dashed box), rather than a regular distribution and a specific angle.

Furthermore, Fig. 18 illustrates the statistics of SDB spacing during evolution. It was observed that the dis-
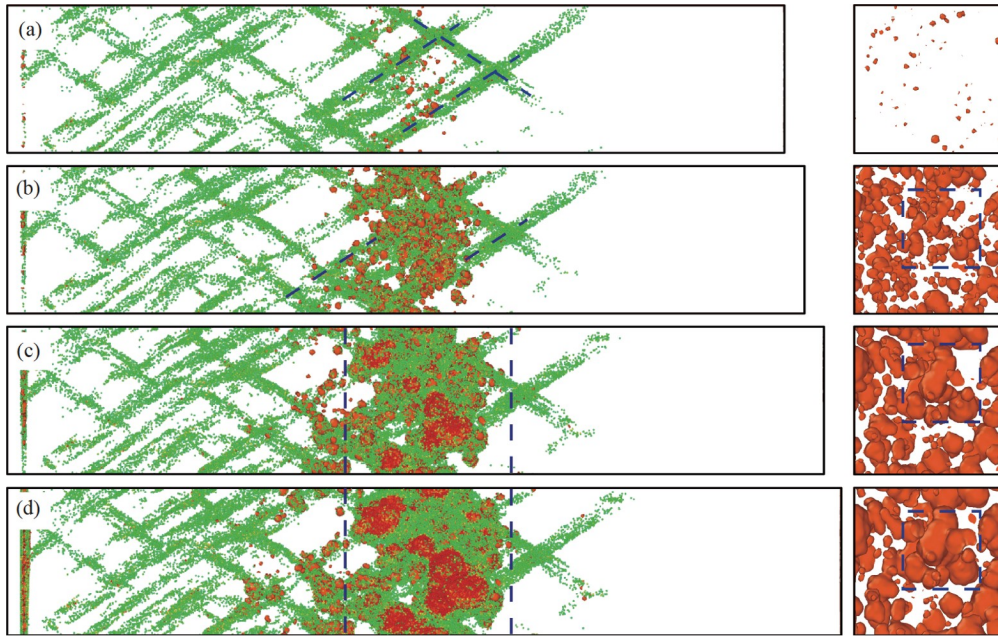
Figure 15 Schematic of the interaction between void growth and SDBs at (a) 28, (b) 30, (c) 32, and (d) 34 ps when the impact velocity is 1.0 km/s.
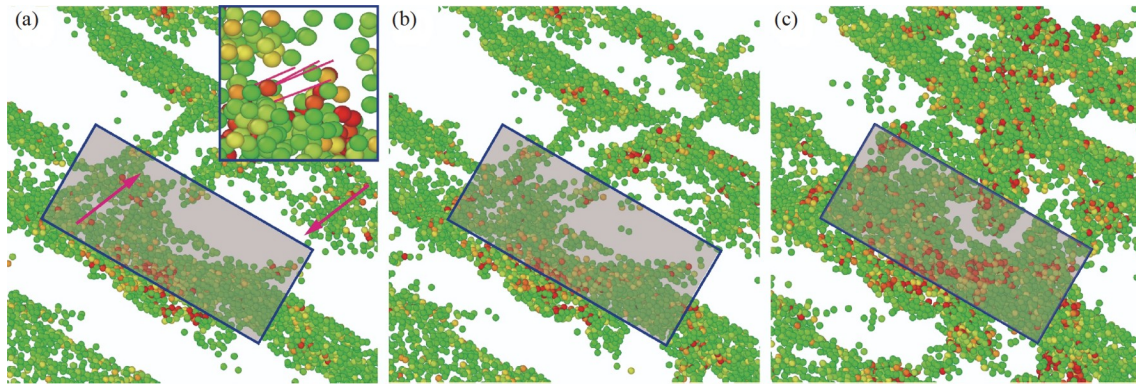

Figure 16 SDB broadening at (a) 27, (b) 28, and (c) 29 ps, when the impact velocity is 1.0 km/s.

tribution pattern of SDB remains almost unchanged during the dislocation diffusion and annihilation in the SDB, demonstrating that there is a pinning effect of dislocations [52]. After dislocation annihilation, such an effect is weakened so that the SDB becomes wider. As has been mentioned earlier, the presence of SDBs affects void nucleation/growth path and mode. On the contrary, the SDB coalescence occurs during void evolution, altering the distribution pattern of SDBs. Accordingly, the void evolution plays a contributing role in SDB broadening.

4.   Conclusion

This work focused on exploring the dynamic response of single-crystal NiTi alloys damaged by shear localization. The NEMD method together with the EAM potential was

used to successfully reproduce the propagation, reflection, and interaction of shock waves. According to shear stress and particle velocity profiles, the simulated system was found to be divided into plastic, elastic, and unshocked regions. Plastic regions correspond to the survival of SDBs colored according to shear strain. Interestingly, no SDBs are generated in the material when the impact velocity is less than 0.75 km/s. In contrast, considerable SDBs appear in the samples. The average spacing between SDBs decreases when increasing the impact velocity to 1.2 km/s. After the formation of SDBs, they continuously expand along the shock direction until the maximum distribution area is reached.

Second, the influence of dislocations on the evolution of SDBs is revealed by quantitatively analyzing the length and distribution region of dislocations. Additionally, we observed that dislocations are clustered around SDBs and
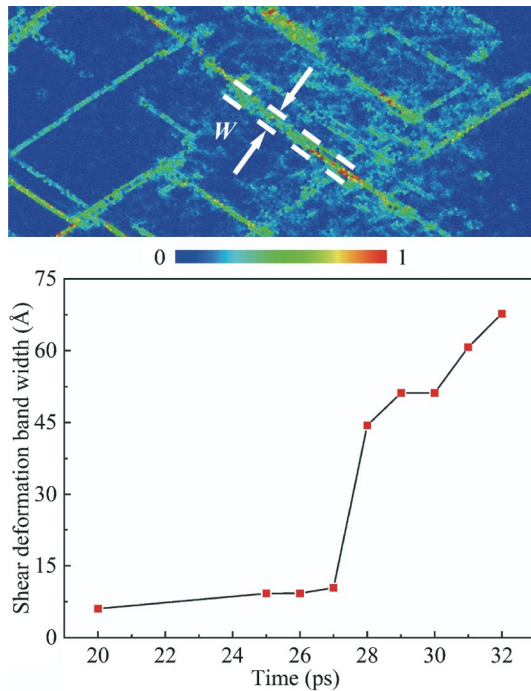
Figure 17 Variation of SDB width with time during the broadening at the impact velocity of 1.0 km/s.
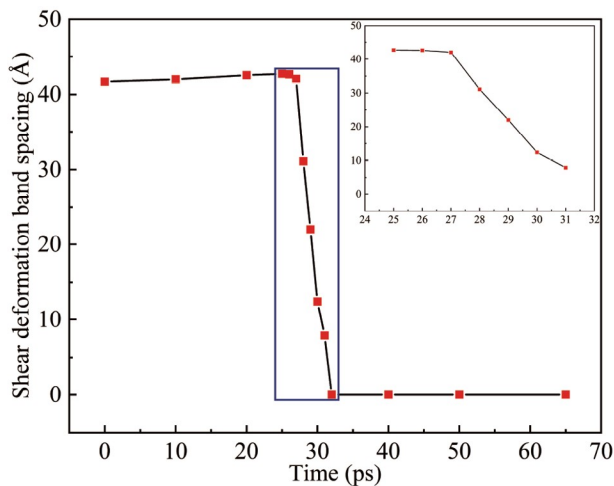

Figure 18 Variation of the spacing of SDB with time at the impact velocity of 1.0 km/s.

propagated in the sample. In this study, the plastic deformation was mainly represented by $\langle 100 \rangle$ partial dislocations. For the case with no SDBs, there were dominant $1/2\langle 111 \rangle$ full dislocations within the material. Thus, the types of dislocations are affected by SDBs. Over time, there is an increase in dislocation length, leading to a decrease in the distance between dislocations. When such a distance is small enough, two dislocations with equal and opposite Burgers vectors cancel each other and are annihilated. Further, the presence of SDB promotes the dislocation-type transformation from $1/2\langle 111 \rangle$ to $\langle 100 \rangle$. Because there is no

significant change in distribution characteristics of the SDBs when dislocations survive, it is believed that dislocations have a pinning effect on the evolution of SDBs. After dislocations are annihilated, voids begin to be nucleated and then grow.

Furthermore, we found that voids are likely to be nucleated on SDBs. The void growth promotes a change in the SDB distribution characteristics from a regular strip with a fixed angle to the bulk pattern. In contrast, further observations demonstrate that void nucleations occur randomly and that the voids tend to grow in a non-uniform manner in the materials for no SDBs. There is an interaction between SDBs and voids in the NiTi alloy at a high strain rate.

1   J. Wang, Z. Moumni, and W. Zhang, A thermomechanically coupled finite-strain constitutive model for cyclic pseudoelasticity of polycrystalline shape memory alloys, Int. J. Plast. **97**, 194 (2017).

2   J. Mohd Jani, M. Leary, A. Subic, and M. A. Gibson, A review of shape memory alloy research, applications and opportunities, Mater. Des. (1980-2015) **56**, 1078 (2014).

3   M. Elahinia, N. Shayesteh Moghaddam, M. Taheri Andani, A. Amerinatanzi, B. A. Bimber, and R. F. Hamilton, Fabrication of NiTi through additive manufacturing: A review, Prog. Mater. Sci. **83**, 630 (2016).

4   M. A. Meyers, and C. Taylor Aimone, Dynamic fracture (spalling) of metals, Prog. Mater. Sci. **28**, 1 (1983).

5   D. K. Kim, S. Lee, and W. Hyung Baek, Microstructural study of adiabatic shear bands formed by high-speed impact in a tungsten heavy alloy penetrator, Mater. Sci. Eng.-A **249**, 197 (1998).

6   Q. Wei, T. Jiao, K. T. Ramesh, E. Ma, L. J. Kecskes, L. Magness, R. Dowding, V. U. Kazykhanov, and R. Z. Valiev, Mechanical behavior and dynamic failure of high-strength ultrafine grained tungsten under uniaxial compression, Acta Mater. **54**, 77 (2006).

7   F. Zhao, Nature of ductile shear banding under shock loading, Micro Nano Lett. **16**, 359 (2021).

8   S. Liao, and J. Duffy, Adiabatic shear bands in a TI-6Al-4V titanium alloy, J. Mech. Phys. Solids **46**, 2201 (1998).

9   X. Ma, D. Zhao, S. Yadav, D. Sagapuram, and K. Y. Xie, Grain-subdivision-dominated microstructure evolution in shear bands at high rates, Mater. Res. Lett. **8**, 328 (2020).

10   T. Wang, Z. L. Liu, Y. N. Cui, X. Ye, X. M. Liu, R. Tian, and Z. Zhuang, A thermo-elastic-plastic phase-field model for simulating the evolution and transition of adiabatic shear band. Part II. Dynamic collapse of thick-walled cylinder, Eng. Fract. Mech. **231**, 107027

(2020).

11　Q. Zeng, M. Chen, X. Yu, W. Qi, S. Zhu, H. Yang, and H. S. Chen, Two-dimensional evolution of temperature and deformation fields during dynamic shear banding: In-situ experiments and modeling, Int. J. Plast. **171**, 103782 (2023).

12　P. Wen, G. Tao, D. E. Spearot, and S. R. Phillpot, Molecular dynamics simulation of the shock response of materials: A tutorial, J. Appl. Phys. **131**, 051101 (2022).

13　K. E. Avila, S. Küchemann, and H. M. Urbassek, Interaction between parallel shear bands in a metallic glass, J. Non-Crystalline Solids **566**, 120882 (2021).

14　Y. Xu, and J. Chen, Atomistic potentials based energy flux integral criterion for dynamic adiabatic shear banding, J. Mech. Phys. Solids **75**, 45 (2015).

15　B. L. Holian, and P. S. Lomdahl, Plasticity induced by shock waves in nonequilibrium molecular-dynamics simulations, Science **280**, 2085 (1998).

16　B. Gurrutxaga-Lerma, Adiabatic shear banding and the micromechanics of plastic flow in metals, Int. J. Solids Struct. **132-133**, 153 (2018).

17　V. Tvergaard, and A. Needleman, Analysis of the cup-cone fracture in a round tensile bar, Acta Metall. **32**, 157 (1984).

18　Y. Sun, C. Wang, W. Wang, T. Li, and T. Yang, Dynamic response analysis of a small-scaled ACLNG storage tank under penetration and explosion loadings, Acta Mech. Sin. **39**, 123110 (2023).

19　W. P. Wu, Z. Peng, D. Șopu, and J. Eckert, Molecular dynamics study of fracture and plastic deformation of Cu/Cu64Zr36 crystalline/amorphous composites with a pre-existing void, J. Non-Crystalline Solids **586**, 121556 (2022).

20　D. V. Kubair, K. T. Ramesh, and P. K. Swaminathan, Effect of shear-void-growth-softening on adiabatic shear-band-spacing in ductile materials, Acta Mech. **226**, 4189 (2015).

21　C. Bil, K. Massey, and E. J. Abdullah, Wing morphing control with shape memory alloy actuators, J. Intell. Mat. Syst. Str. **24**, 879 (2013).

22　L. Shen, Y. Liu, and M. Hui, Dynamic thermo-mechanical behaviors of SME TiNi alloys subjected to shock loading, Acta Mech. Sin. **36**, 1336 (2020).

23　X. Zhang, G. Wang, B. Luo, S. N. Bland, F. Tan, F. Zhao, J. Zhao, C. Sun, and C. Liu, Mechanical response of near-equiatomic NiTi alloy at dynamic high pressure and strain rate, J. Alloys Compd. **731**, 569 (2018).

24　J. Wang, F. Wang, X. Zeng, Z. Qi, X. Yang, G. Xie, and Z. Xu, Unraveling the plasticity performance and melting in single crystal tantalum damaged by shock compression, Eng. Fract. Mech. **276**, 108921 (2022).

25　J. Wang, F. Wang, X. Wu, Z. Xu, and X. Yang, Orientation-induced anisotropy of plasticity and damage behavior in monocrystalline tantalum under shock compression, Vacuum **207**, 111679 (2023).

26　K. Mackenchery, R. R. Valisetty, R. R. Namburu, A. Stukowski, A. M. Rajendran, and A. M. Dongare, Dislocation evolution and peak spall strengths in single crystal and nanocrystalline Cu, J. Appl. Phys. **119**, 044301 (2016).

27　X. Wu, F. Wang, J. Wang, X. Yang, X. Zeng, H. Zhang, C. Lv, and X. Pei, Correlation between grain size and dynamic response of NiTi alloy during intense shock-induced multi-spallation, Mater. Today Commun. **37**, 107515 (2023).

28　Y. Zhong, K. Gall, and T. Zhu, Atomistic study of nanotwins in NiTi shape memory alloys, J. Appl. Phys. **110**, 033532 (2011).

29　W. S. Lai, and B. X. Liu, Lattice stability of some Ni-Ti alloy phases versus their chemical composition and disordering, J. Phys.-Condens. Matter **12**, L53 (2000).

30　N. Hatcher, O. Y. Kontsevoi, and A. J. Freeman, Role of elastic and shear stabilities in the martensitic transformation path of NiTi, Phys. Rev. B **80**, 144203 (2009).

31　M. Lu, F. Wang, X. Zeng, W. Chen, and J. Zhang, Cohesive zone modeling for crack propagation in polycrystalline NiTi alloys using molecular dynamics, Theor. Appl. Fract. Mech. **105**, 102402 (2020).

32　M. I. Baskes, Modified embedded-atom potentials for cubic materials and impurities, Phys. Rev. B **46**, 2727 (1992).

33　O. Mercier, K. N. Melton, G. Gremaud, and J. Hägi, Single-crystal elastic constants of the equiatomic NiTi alloy near the martensitic transformation, J. Appl. Phys. **51**, 1833 (1980).

34　E. N. Hahn, and S. J. Fensin, Influence of defects on the shock Hugoniot of tantalum, J. Appl. Phys. **125**, 215902 (2019).

35　S. Plimpton, Fast parallel algorithms for short-range molecular dynamics, J. Comput. Phys. **117**, 1 (1995).

36　C. Lv, X. P. Zhang, G. J. Wang, F. Zhao, N. Luo, S. N. Bland, F. L. Tan, J. H. Zhao, C. L. Liu, and C. W. Sun, Twinning and rotational deformation of nanocrystalline NiTi under shock loading, Phys. Rev. Mater. **4**, 093607 (2020).

37　S. Volz, J. B. Saulnier, G. Chen, and P. Beauchamp, Computation of thermal conductivity of Si/Ge superlattices by molecular dynamics techniques, MicroElectron. J. **31**, 815 (2000).

38　D. Wu, Y. Zhu, L. Zhao, M. Huang, and Z. Li, Atomistic investigation of mechanical response and deformation mechanism of BCC Ta under double shock loading, J. Appl. Phys. **129**, 175110 (2021).

39　P. Li, Y. Huang, K. Wang, S. Xiao, L. Wang, S. Yao, W. Zhu, and W. Hu, Crystallographic-orientation-dependence plasticity of niobium under shock compressions, Int. J. Plast. **150**, 103195 (2022).

40　S. N. Luo, Q. An, T. C. Germann, and L. B. Han, Shock-induced spall in solid and liquid Cu at extreme strain rates, J. Appl. Phys. **106**, 013502 (2009).

41　Y. J. He, and B. Ma, Molecular dynamics analysis on bending mechanical behavior of alumina nanowires at different loading rates, T. Nonferr. Metal. Soc. **32**, 3687 (2022).

42　W. Chen, Y. Liu, D. Qu, M. Zheng, Q. Lang, S. Zhu, and Z. Zhu, Effect of pores on microscopic wear properties and deformation behavior of Ni-Cr alloy coating, J. Mol. Model. **29**, 330 (2023).

43　Z. Qi, L. He, F. Wang, J. Wang, J. Cheng, G. Xie, and X. Zeng, Role of temperature and strain rate on the stress reversal in dynamic damage of monocrystalline NiTi alloy, Mech. Mater. **165**, 104185 (2022).

44　A. Singla, and A. Ray, Hugoniot elastic limit of single-crystal tantalum at normal and elevated temperatures subjected to extreme strain rates, Phys. Rev. B **105**, 064102 (2022).

45　N. Wang, I. K. Sou, and K. K. Fung, Transmission electron microscopy study of stacking faults and the associated partial dislocations in pseudomorphic epilayers of ZnSe/GaAs(001), J. Appl. Phys. **80**, 5506 (1996).

46　F. Yazdandoost, and R. Mirzaeifar, Generalized stacking fault energy and dislocation properties in NiTi shape memory alloys, J. Alloys Compd. **709**, 72 (2017).

47　T. W. Wright, and R. C. Batra, The initiation and growth of adiabatic shear bands, Int. J. Plast. **1**, 205 (1985).

48　D. D. Alix-Williams, and M. L. Falk, Shear band broadening in simulated glasses, Phys. Rev. E **98**, 053002 (2018).

49　T. Huang, F. Liu, Z. Liu, G. He, and Y. Hu, Dislocation multiplication and dynamics in an aluminium alloy, Philos. Mag. Lett. **102**, 209 (2022).

50　H. Saka, Toughening of a brittle material by means of dislocation subboundaries, Philos. Mag. Lett. **80**, 461 (2000).

51　L. He, F. Wang, X. Zeng, X. Yang, and Z. Qi, Atomic insights into shock-induced spallation of single-crystal aluminum through molecular dynamics modeling, Mech. Mater. **143**, 103343 (2020).

Y. Zhang, *et al. Acta Mech. Sin.*, Vol. 41, 124177 (2025)

124177-12

52 T. Tokuzumi, M. Mitsuhara, S. Yamasaki, T. Inamura, T. Fujii, and H. Nakashima, Role of disclinations around kink bands on deformation behavior in Mg-Zn-Y alloys with a long-period stacking ordered phase, Acta Mater. **248**, 118785 (2023).

剪切局域化诱导的单晶NiTi合金动态损伤响应

张玉辰, 杨伟龙, 杨鑫, 王进, 吕超, 张豪, 裴晓阳, 王放

摘要　本研究利用非平衡分子动力学模拟方法, 从原子尺度探讨了单晶镍钛合金的动态响应. 结果表明: 当冲击速度小于0.75 km/s时, 材料内部没有出现剪切变形带. 随着速度增加, 剪切变形局域化现象愈发显著, 并且这种变形带的平均间距逐渐减小直至没有明显变化. 结合剪切应力及粒子速度分布曲线, 可以认为剪切变形带的存在与塑性变形紧密相关. 此外, 团簇在剪切变形带周围的位错以 $\langle 100 \rangle$ 部分位错为主: 在没有剪切变形带的区域, $1/2\langle 111 \rangle$ 全位错占主导地位. 孔洞形核主要发生在剪切变形带上, 随后, 孔洞长大促进了剪切变形带分布特征变化. 对于没有剪切变形带的情况, 孔洞随机形核, 此时孔洞增长呈现出不均匀方式. 因此, 强动载荷下镍钛合金的损伤过程伴随着剪切局域化和孔洞的演化及其相互作用. 本工作有助于深入揭示镍钛合金动态损伤的微观机理.